

1 **Sea surface height anomalies of the Arctic Ocean from ICESat-2: a first examination**
2 **and comparisons with CryoSat-2**

3
4 **M. Bagnardi^{1,2}, N. Kurtz¹, A. A. Petty^{1,3}, R. Kwok⁴**

5 ¹Cryospheric Sciences Laboratory, NASA Goddard Space Flight Center, Beltsville, MD, United
6 States.

7 ²ADNET Systems, Inc., Bethesda, MD, United States.

8 ³Earth System Interdisciplinary Center, University of Maryland, College Park, MD, United
9 States.

10 ⁴Polar Science Center, Applied Physics Laboratory, University of Washington, Seattle, WA,
11 United States.

12
13
14 Corresponding author: Marco Bagnardi (marco.bagnardi@nasa.gov)

15
16 **Key Points:**

- 17 • We present the first (multi-year) examination of Arctic Ocean sea surface height
18 anomalies (SSHA) from the ICESat-2 laser altimeter.
- 19 • ICESat-2 SSHA estimates compare well with near-coincident (*CRYO2ICE*) radar
20 altimetry-derived SSHA estimates from CryoSat-2.
- 21 • ICESat-2 and CryoSat-2 show good agreement in the seasonal variability in SSHA
22 suggesting ICESat-2 adds to the time-series of Arctic SSHA.

23 Abstract.

24 Accurately resolving spatio-temporal variations in sea surface height across the polar
25 oceans is key to improving our understanding of ocean circulation variability and change. Here,
26 we examine the first two years (2018-2020) of Arctic Ocean sea surface height anomalies
27 (SSHA) from the photon-counting laser altimeter onboard NASA's ICE, Cloud, and Land
28 Elevation Satellite-2 (ICESat-2). ICESat-2 SSHA estimates are compared to independent
29 estimates from the CryoSat-2 mission, including available semi-synchronous along-track
30 measurements from the recent *CRYO2ICE* orbit alignment campaign. There are documented
31 residual centimeter-scale range biases between the ICESat-2 beams (in the current data release,
32 r003) and we opted for a single-beam approach in our comparisons. We find good agreements in
33 the along-track estimates (correlations > 0.8 and differences < 0.03 m) as well as in the gridded
34 monthly SSHA estimates (correlation 0.76 and mean difference 0.01 m) from the two altimeters,
35 suggesting ICESat-2 adds to the SSHA estimates from CryoSat-2.

36

37 Plain Language Summary

38 The polar oceans, with warming and dramatic declines in sea ice coverage, are experiencing
39 some of the most rapid environmental changes on Earth. These changes have direct impacts on
40 ocean circulation and freshwater distribution, with observable changes in sea surface height.
41 Measuring and monitoring basin-scale variability of sea level of the ice-covered oceans has
42 proven challenging because the surface of these oceans is only exposed within narrow openings
43 in the sea ice, requiring high spatial resolution and bespoke measurement techniques. This study
44 takes a first look at new high-resolution laser altimetry measurements of sea level over the Arctic
45 Ocean collected by NASA's ICESat-2 satellite since its launch in 2018. We compare the results

46 with those obtained using independent data from the CryoSat-2 satellite radar altimeter. By
47 looking at near-synchronous data from when the orbit of the two satellites coincide over the
48 Arctic Ocean, and by comparing sea surface height maps from both sensors during the two years
49 of overlap (2018-2020) between the two missions, we find good agreement between the sea
50 surface height estimates, providing additional confidence that ICESat-2 can be used to infer
51 regional and seasonal polar sea surface height variability.

52 **1 Introduction**

53 Satellite observations of the Arctic Ocean have shown significant changes in ocean
54 circulation, fresh water storage and energy balance since at least the 1980s, (Armitage et al.,
55 2020; Morison et al., 2012, 2021; Polyakov et al., 2017; Proshutinsky et al., 2019; Timmermans
56 & Marshall, 2020). Routine and accurate profiling of the sea surface height (SSH) in the Arctic is
57 needed to continue these crucial time-series and provide more detailed insights into these
58 changes. While we can reliably monitor the sea surface height of the open oceans at low-to-mid
59 latitudes using satellite altimetry data (IPCC, 2019), continuous and widespread measurements at
60 high-latitude ice-covered seas have remained limited. The main challenges are the reduced
61 coverage due to the low inclination orbit of most satellite altimeters, sea surface sampling limited
62 to narrow openings in the sea ice cover, and the need to accurately discriminate between sea ice
63 and ocean surface altimetry returns.

64 Measurements of Arctic SSH from satellite altimetry started with low resolution radar
65 data collected by the European Space Agency's (ESA) ERS and Envisat radar missions (1995–
66 2010; Giles et al., 2012; Peacock & Laxon, 2004). However, the orbit inclination of these
67 satellites limited measurements to 81.5° latitude. NASA's ICESat satellite, which operated
68 between 2003 and 2009 (Zwally et al., 2002), offered higher resolution lidar data that improved

69 lead classification and SSH estimates (Kwok & Morison, 2011) while its orbit inclination
70 resulted in more extensive coverage of the Arctic Ocean. Since 2010, ESA's CryoSat-2 satellite
71 has been acquiring unfocussed synthetic aperture radar (SAR) altimetry data over the polar
72 regions. CryoSat-2's high orbit inclination and continuous data collection have enabled basin-
73 scale mapping of seasonal and interannual SSH variability up to 88° latitude (Wingham et al.,
74 2006). The SSH data from CryoSat-2 have been compared with Arctic tide gauge measurements
75 and ocean mass variations (e.g., GRACE) and basin-scale, monthly, estimates of dynamic ocean
76 topography (DOT; Armitage et al., 2016, 2018; Kwok & Morison, 2016) have been produced.

77 In September 2018, NASA launched the Ice, Cloud, and Land Elevation Satellite-2
78 (ICESat-2) laser altimetry mission, which has since been providing year-round profiling of the
79 Earth's surface up to 88° latitude (Neumann et al., 2019). The novel photon-counting Advanced
80 Topographic Laser Altimeter (ATLAS) on ICESat-2 provides high-resolution surface height
81 measurements across its six-beam configuration. For the polar oceans, the data collected by
82 ICESat-2 are currently being used to produce routine estimates of sea ice height, type (e.g.,
83 lead/ice), and freeboard (Kwok et al., 2020). The ICESat-2 processing algorithms utilize specular
84 returns to discriminate open-water leads from sea ice, and the laser's spatial resolution (~11 m
85 diameter footprint; Magruder et al., 2020) is significantly higher than that of CryoSat-2 (380 m
86 along-track and 1650 m across-track pulse limited footprint; Scagliola, 2013). Also,
87 contamination by off-nadir specular returns from up to 15 km across-track can potentially bias
88 CryoSat-2 surface height retrievals (Armitage & Davidson, 2014). On the other hand, laser
89 altimetry measurements are often hindered by the presence of clouds, which are otherwise
90 penetrated by radar. Measurements of sea ice height and freeboard by ICESat-2 have been
91 validated against coincident laser profiles collected during targeted underflights by NASA's

92 Operation IceBridge (OIB) airborne mission (Kwok et al., 2019) and the sea ice classification
93 algorithm has been shown to agree well with coincident imagery (R. Kwok et al., 2021; Petty et
94 al., 2021). At the time of writing, sea surface height measurements have yet to be compared
95 against independent height data.

96 As of August 2020, the orbit of CryoSat-2 has been modified as part of the *CRYO2ICE*
97 campaign, such that every 19 orbits (20 orbits for ICESat-2) the two satellites are aligned for
98 hundreds of kilometers over the Arctic Ocean, acquiring data along near-coincident ground
99 tracks with a minimum time difference of approximately three hours. In this study, we present a
100 first comparison of semi-synchronous along-track SSHA retrievals from ICESat-2 and CryoSat-2
101 from several *CRYO2ICE* profiles. We examine SSHA from individual ICESat-2 beams and
102 assess inter-beam range biases. We produce gridded SSHA composite maps of the Arctic Ocean
103 and examine the relative agreement of the monthly, seasonal, and multi-year SSHA from the two
104 altimeters. Daily/monthly gridded SSHA measurements over both polar oceans are planned to be
105 released as an official ICESat-2 data product (ATL21) in 2021, and this study offers an
106 examination of this type of composite SSHA data over the Arctic.

107 **2 Data and Methods**

108 *2.1 ICESat-2 data*

109 The ICESat-2 photon-counting laser altimeter transmits laser pulses split into a six-beam
110 configuration of three beam pairs (each having a strong and a weak beam), where beam numbers
111 1, 3, and 5 identify the strong beams, and 2, 4, and 6 the weak beams (Neumann et al., 2019).
112 The 10 kHz pulse repetition rate leads to a 0.7 m along-track separation between subsequent
113 laser pulses of the ~11 m lidar footprint (Magruder et al., 2020). Among the ICESat-2 data

114 products, the Level 3A sea ice products ATL07 (sea ice height and type,
115 <https://nsidc.org/data/ATL07>) and ATL10 (freeboard, <https://nsidc.org/data/ATL10>) provide
116 along-track measurements for six individual ground tracks (targeted at reference ground tracks,
117 RGTs), and up to 16 satellite passes per day over both the Arctic and the Southern Ocean. The
118 along-track surface heights are generated by aggregating 150 geolocated signal photon heights
119 from the primary science Level 2A ATL03 data product (Neumann et al., 2019). ATL10 data
120 coverage is limited to areas that have an ice concentration $> 50\%$ (15% for ATL07), as inferred
121 from passive microwave satellite measurements, and up to 25 km distance from land. A full
122 description of the ATL07/10 products can be found in the Algorithm Theoretical Basis
123 Document (ATBD, Kwok et al., 2020) and recent changes to the algorithm are further discussed
124 in (Kwok et al., 2021). In this study we use release 003 (r003) ATL10 data.

125 In ATL10, the SSHA represents the measured sea surface elevation relative to a multi-
126 year mean sea surface (MSS, see Section 2.3) after various geophysical and atmospheric
127 corrections have been applied (see Table S1). Note that we adjust the solid earth tide correction
128 included in each ICESat-2 segment's SSHA from r003 ATL10 data to correct a discrepancy in
129 the permanent tide system. The adjustment is described in the supporting information (Text S1).
130 The SSHA is provided for each beam at three different length-scales: (1) the
131 *height_segment_height* variable where *ssh_flag* = 1 or 2 (height segments classified as sea
132 surface after radiometric classification as specular returns and height filtering), provides SSHA
133 measurements calculated from the Gaussian fit to the height distribution of 150 photons within a
134 segment (~ 7 m mean along-track SSH segment length for strong beams); (2) *lead_height*,
135 expresses the weighted mean height from consecutive segments forming an individual lead; (3)
136 *beam_refsurf_height*, represents the SSHA for a ~ 10 -km along-track section, calculated as the

137 weighted mean of all leads within a given section for each beam, or linearly interpolated from
138 two adjacent sections, and smoothed using a 3-point point smoother. In subsequent analyses we
139 use (1) but note that ATL21 data products will be formed using (3) to be consistent with the
140 reference sea surface heights used to calculate freeboards (ATL10 and ATL20). This choice does
141 not introduce significant differences in the gridded SSHA estimates (not shown) but allows us to
142 take advantage of higher spatial resolution and of non-interpolated data when comparing results
143 with CryoSat-2.

144 *2.2 CryoSat-2 data*

145 We use data acquired by the SIRAL K_u band SAR altimeter in the SAR mode, one of
146 CryoSat-2's three modes of operation. We use intermediate Level 2 (L2) ice products processed
147 at Baseline-D (Meloni et al., 2020) and available from ESA's CryoSat-2 Science Server
148 (<https://science-pds.cryosat.esa.int/>). L2 data provide geolocated height measurements above the
149 reference ellipsoid (WGS84) computed from each echo at intervals of approximately 300 meters.
150 The data are already corrected for instrument effects, propagation delays, measurement
151 geometry, and other geophysical effects (e.g., atmospheric delays and tides, see Table S1).
152 Waveform retracking is also already applied in L2 data and determined using a model-fitting
153 method to specular lead waveforms described by Giles et al. (2007). Further details and
154 information can be found in the CryoSat-2 Baseline D Product Handbook (ESA, 2019) and in
155 Meloni et al. (2020). Data coverage is controlled by the operational geographical mode mask for
156 SAR data (<https://earth.esa.int/web/guest/-/geographical-mode-mask-7107>) and updated weekly
157 to account for changes in sea-ice extent.

158 2.3 Mean sea surface (MSS)

159 To consistently compute the SSHA for CryoSat-2 we remove a mean sea surface height
160 from each ellipsoidal elevation from L2 data (*height_sea_ice_lead_20_ku*, which includes all
161 instrumental and geophysical corrections) by bilinearly interpolating MSS values from a 2.5 km
162 grid (Kwok et al., 2020 – <https://zenodo.org/record/4294048>) to the interval centroids. The MSS
163 grid and the interpolation approach are the same as those used in the ICESat-2 sea ice data
164 products. The MSS includes the geoid component and is in the mean-tide system.

165 2.4 SSHA data binning and gridding

166 In along-track comparisons for the *CRYO2ICE* campaign (Figure 1, Section 3.1), we first
167 identify measurement overlaps by selecting ICESat-2 SSHA segments from a given beam that
168 fall within the theoretical CryoSat-2 pulse-limited across-track footprint (± 825 m across-track
169 from the centroid of each footprint; Scagliola, 2013). We then bin individual SSHA segments for
170 ICESat-2 and SSHA intervals for CryoSat-2 in coincident 10-km sections and calculate the
171 simple mean value from all measurements within each bin (shown as stars in Figure 1). For each
172 profile we calculate the mean (μ) and standard deviation (SD) of the differences from all bins,
173 and the correlation coefficient (R) between the two datasets.

174 To generate composite maps of the Arctic Ocean SSHA, along-track data from ICESat-2
175 and CryoSat-2 are first reprojected from the WGS 84 (EPSG:4326) to the NSIDC Sea Ice Polar
176 Stereographic North coordinate system (EPSG:3411). The SSHA data are then gridded to the 25-
177 km SSM/I polar stereographic grid by calculating the mean value within each grid cell for all
178 data acquired within a given time period. Finally, we apply to both datasets a mask based on the
179 NSIDC Arctic regional mask, in order to limit our assessment to the Beaufort, Chukchi, East

180 Siberian, Laptev, Kara, Barents, and Greenland seas, and the Central Arctic (see Figure S1 and
181 black dashed outline in maps shown in Figure 2-4).

182 **3 Results and discussion**

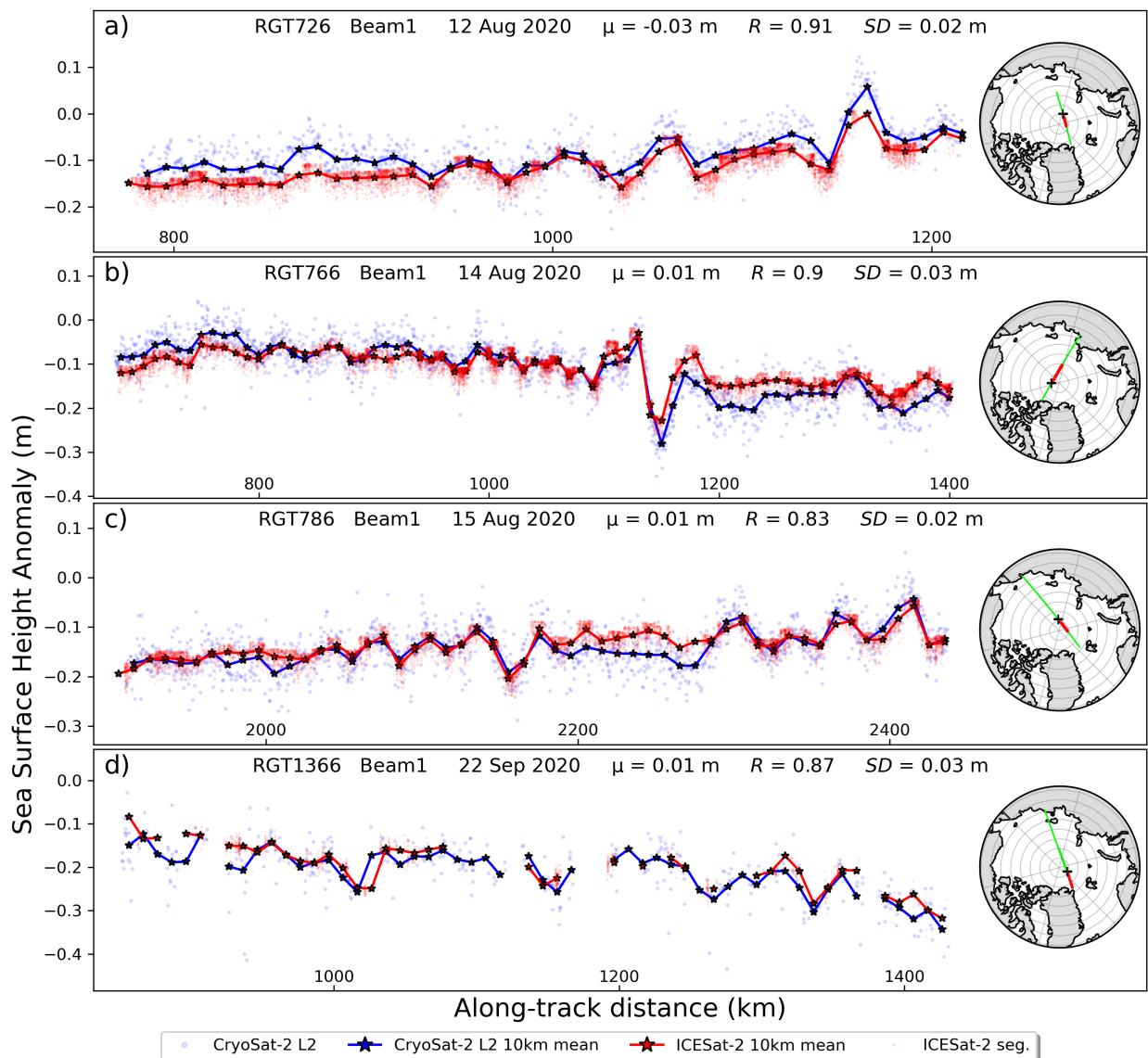
183 *3.1 Along-track CRYO2ICE SSHA comparison*

184 There have been 77 nominal orbit overlaps between ICESat-2 and CryoSat-2 since the
185 start of the *CRYO2ICE* campaign on 4 August 2020 (ICESat-2 RGT 606) and 11 November
186 2020 (ICESat-2 RGT 739), the date of the last ICESat-2 r003 ATL10 dataset available at
187 NSIDC. For some overlaps the data products are not available and for many other overlaps, data
188 are missing/invalid (e.g., because of cloud cover in ICESat-2). From the subset of available data,
189 we find 4 overlaps that extend for at least 400 km with >1000 valid sea surface height
190 segments/intervals. Most overlaps over the Arctic Ocean, including those in our subset, are with
191 ICESat-2's beam 1 (*gt11*). Note that the first three overlaps in our subset (Figure 1a-c) occur
192 within summer, and while there are possible benefits from a higher lead fraction and increased
193 number of SSH segments/intervals, we recognize that the presence of melt ponds due to snow
194 melt on sea ice may interfere with the sea surface type retrieval algorithms, especially in the mid-
195 August data when melt ponds are thought to be more prevalent (Kwok et al., 2020; Tilling et al.,
196 2020).

197 Figure 1 shows the along-track SSHA estimates for the four selected *CRYO2ICE* overlaps
198 (12 August to 22 September 2020). Of the four examples, three (14, 15 August and 22
199 September, Figure 1b-d) show mean differences of 0.01 m and one (12 August, Figure 1a) of –
200 0.03 m. The standard deviations are 0.02–0.03 m and the correlation coefficients (R) vary
201 between 0.83 and 0.90. The relative differences between 10-km SSHA sections are shown in

202 Figure S2 together with differences between geophysical corrections (i.e., tides and inverted
 203 barometer). Note that applying the geophysical corrections is key when doing these comparisons,
 204 as the lack of time-coincidence can cause significant (up to 20 cm) differences (Figure S2).

205 The larger (> 0.20 m) SSHA excursion seen in Figure 1b and smaller but still significant
 206 short-scale variability in the other profiles may be localized geoid features (e.g., associated to
 207 deep ocean ridges) that are not represented properly in the current MSS, and unlikely to be ocean
 208 circulation features.



210 **Figure 1:** *CRYO2ICE* along-track SSHA comparisons. Red dots represent ICESat-2 sea
211 surface segments, red stars show the mean value for 10-km sections. Blue dots represent
212 CryoSat-2 sea surface intervals and blue stars the mean value for the same 10-km sections as for
213 ICESat-2. The RGT number identifies the ICESat-2 reference ground track number. The date of
214 acquisition of both datasets (separated by ~ 3 hours) is shown for each panel. For each overlap we
215 report the mean difference (μ), the standard deviation (SD) of differences between the two
216 datasets, and the correlation coefficient R from the least-squares regression. Map insets show the
217 CryoSat-2 ground track in green and the extent of the overlap with ICESat-2 in red. The black +
218 symbol marks the beginning of the profile (left side in main panels).

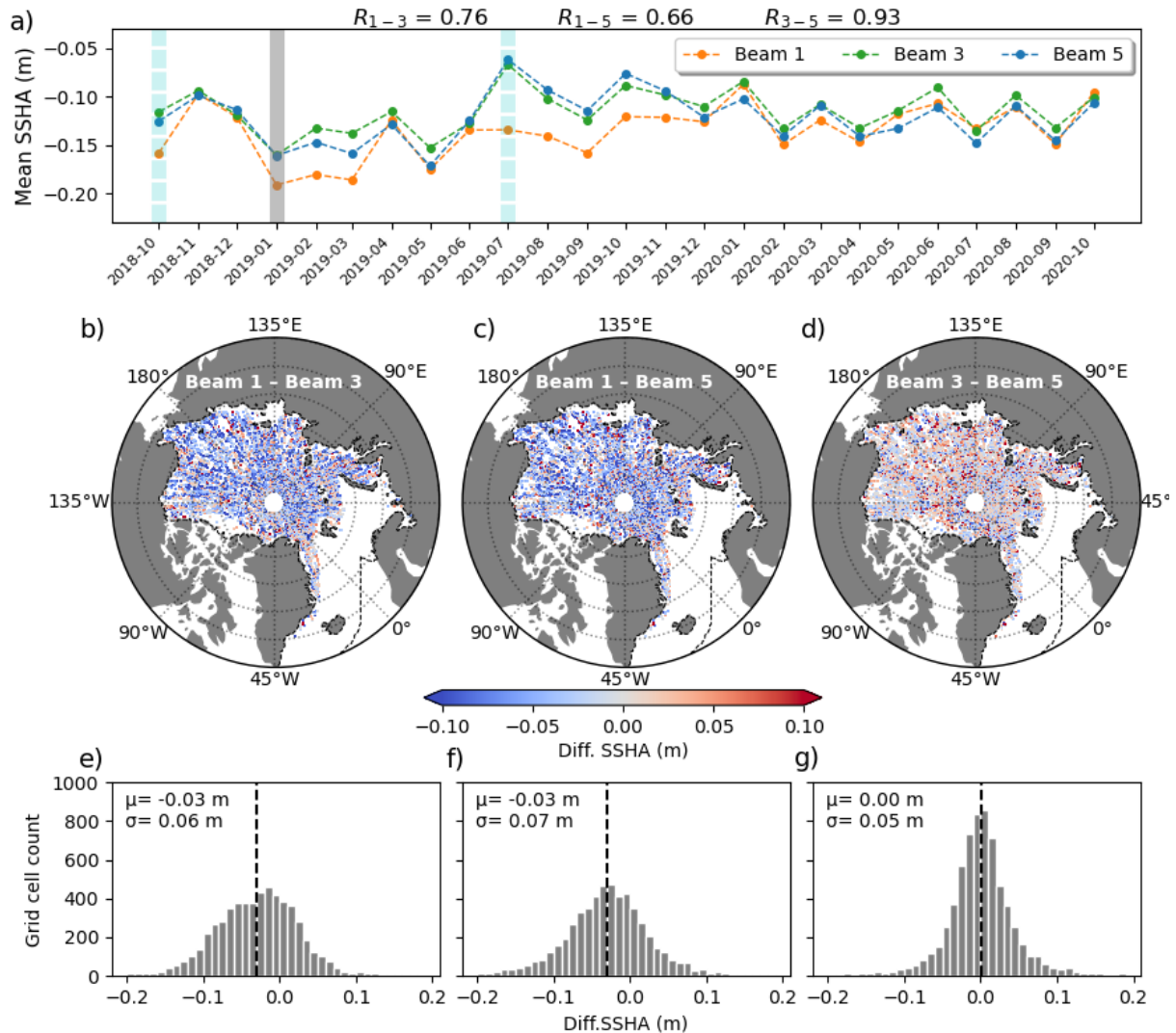
219

220 3.2 ICESat-2 beam comparison

221 Preliminary analyses by the ICESat-2 Project Science Office (PSO) have suggested that
222 the ATLAS beams have different range biases and that these can vary through time – i.e. the
223 height profiles from the 6 beams are not yet fully calibrated/reconciled and centimeter-level
224 differences between beams remain. To understand the inter-beam range variability from SSHA
225 estimates we calculate the monthly mean SSHA value over the Arctic since the start of the
226 mission for the three strong beams independently (Figure 2a). The monthly SSHA estimate from
227 beam 1 presents the largest differences with respect to the two other strong beams (up to ~ 0.07
228 m in July 2019) while differences between beam 3 and beam 5 are consistently ≤ 0.02 m.
229 Correlation coefficients are 0.76, 0.66, and 0.93 for beam 1 – beam 3, beam 1 – beam 5, and
230 beam 3 – beam 5, respectively. In Figure 2b-d we show the spatial distribution of the beam-to-
231 beam differences for a given month (January 2019, gray bar in Figure 2a), which show that
232 differences exhibit no obvious spatial correlation. This remains valid for all months since the
233 start of the mission. The same beam-to-beam differences are also shown as histograms in Figure
234 2e-g, further demonstrating the clear inter-beam bias associated with beam 1 (mean of -0.03 m
235 when compared to beam 3 and 5) and that differences between beam 3 and 5 are normally
236 distributed around a mean of 0.00 m with a standard deviation of 0.05 m. The significant larger
237 differences with beam 1 are also consistent with the findings of Brunt et al. (2021) estimated

238 over the interior ice sheets of Antarctica (beam 1-3: 0.039 m; 1-5: 0.036 m; 3-5: 0.003 m),
239 suggesting that these are sensor- or pointing solution-related.

240 For all of our subsequent analyses (Section 3.3 and 3.4), and until range differences
241 between beams are fully characterized, we opt to use just a single strong beam when estimating
242 Arctic SSHA. Based on the results presented above we select the middle strong beam (beam 3)
243 since, despite its lower transmitted energy level (~80% of beam 1 and 5), the steeper incidence
244 angle results in a stronger backscatter in the presence of highly reflective surfaces (e.g., leads)
245 consistently increasing the number of specular lead returns compared to other strong beams
246 (Kwok et al., 2021). This is currently our recommended strategy for the initial production and
247 release of ICESat-2 ATL21 data.



248

249 **Figure 2:** ICESat-2 beam comparison. **a)** Monthly mean for the Arctic Ocean calculated using
 250 data from each beam. The cyan dashed bars mark months for which data do not cover the entire
 251 month, October 2018–beginning of science data acquisition on 14 October– and July 2019–data
 252 between 1 and 8 July are not available due to satellite safe mode operations. The gray bar marks
 253 the month for which data are shown in panel b-g. Correlation coefficients (R) between beams are
 254 shown at the top. **b-d)** Maps showing the differences between beams for the month of January
 255 2019. The black dashed line marks the extent of the area of interest. **e-g)** histograms showing the
 256 distribution of the differences presented in panels b-d. The black dash lines mark the mean (μ)
 257 and σ is the standard deviation.

258

259

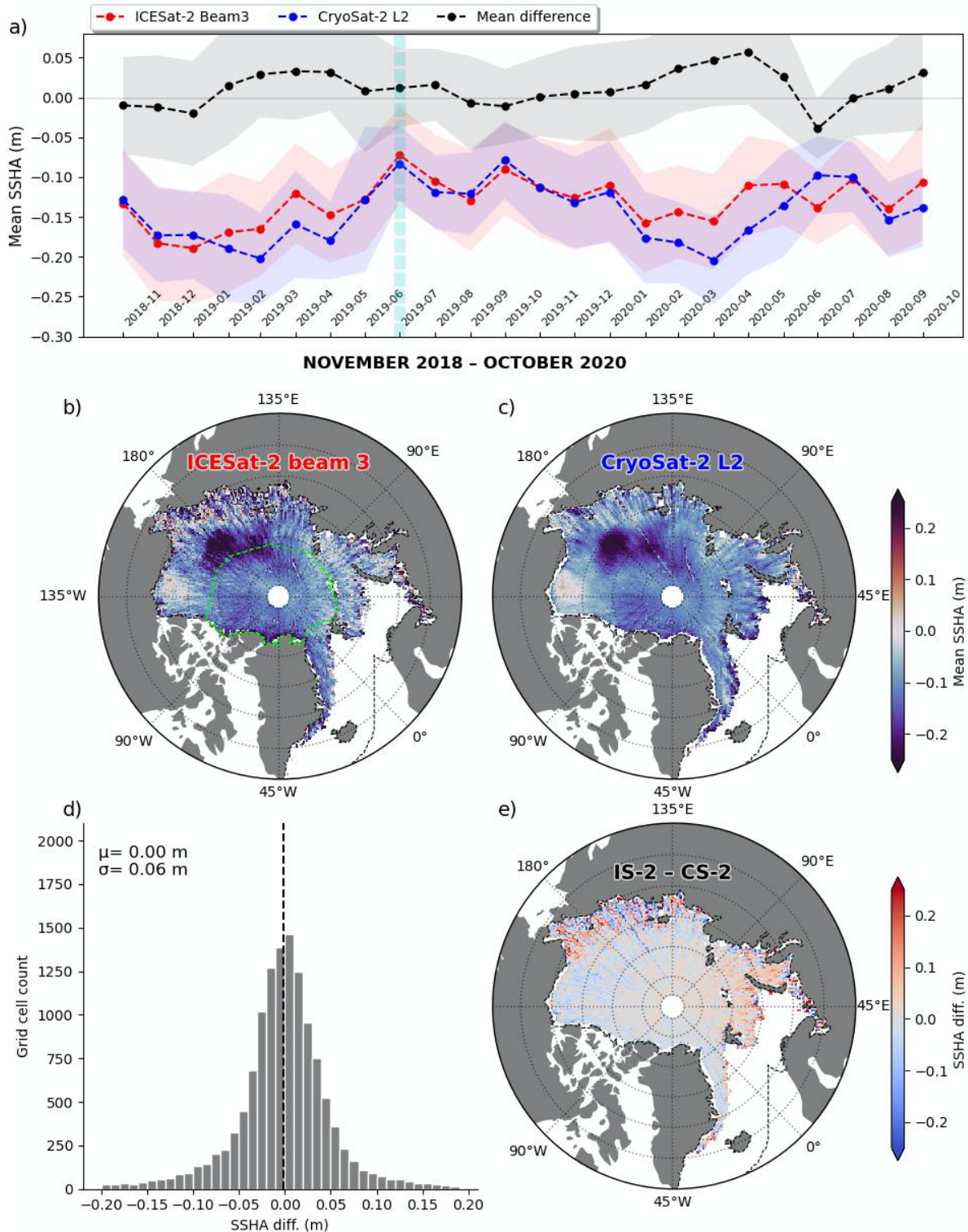
3.3 Monthly and multi-year SSHA comparison

260 In Figure 3a we compare monthly SSHA means calculated using ICESat-2 beam 3 to
261 those calculated using CryoSat-2 Level-2 data. We limit this comparison to the Central Arctic,
262 the area outlined by the green dashed line in Figure 3b, where we expect consistent year-round
263 ice cover and to exclude effects introduced by season-dependent changes in sea-ice extent and
264 different data coverage near the coastal regions. Further details for each monthly comparison
265 (mean, number of valid grid cells, number of data points) are provided in Table S2. A decrease in
266 mean SSHA is shown by both sensors during fall-winter months and is followed by a mean
267 SSHA increase during spring-summer months. Differences across all months between the two
268 sensors have a mean of 0.01 m (SD = 0.02 m), and the correlation coefficient from a least-
269 squares regression (R) is 0.76 (slope = 0.95, intercept = -0.02 m). We find that up to 0.03 m of
270 the observed monthly SSHA differences, especially during fall/winter, are caused by differences
271 in the inverted barometer correction applied to each dataset. Our comparisons between heights
272 from ICESat-2 with those from CryoSat-2 show a better agreement than has been shown by
273 Brunt et al. (2021), who compared absolute ice height over the flat interiors of the Antarctic ice
274 sheet and found differences > 0.3 m. This larger discrepancy, however, is likely due to the much
275 greater penetration depth of the Ku band radar in firn compared to sea water.

276 We then compare the Arctic SSHA calculated from data spanning the two-year mission
277 overlap, from November 2018 through October 2020. The ICESat-2 mean 2018-2020 SSHA in
278 shown in Figure 3b and that from CryoSat-2 is presented in Figure 3c. Both maps show a
279 positive SSHA in the southern Beaufort Sea, a strong negative anomaly in the Chukchi/Siberian
280 seas and a weaker negative SSHA in Central Western Arctic, a spatial pattern consistent with
281 recent positive phase in the Arctic Oscillation (Armitage et al., 2018; Morison et al., 2021). In
282 Figure 3d we show a histogram of the differences between ICESat-2 and CryoSat-2 SSHA, while

283 a map of the SSHA differences is presented in Figure 3e, which shows the ICESat-2 SSHA to be
284 generally higher in the more marginal seas (Barents, Kara, East Siberian, and Chukchi) and
285 slightly lower in the Central Arctic. The marginal seas are areas of large SSH variability where
286 the different acquisition times between the two satellites can capture different parts of these
287 cycles (see Figure S3 for the standard deviation of each dataset, showing higher values in the
288 marginal seas) and can therefore explain much of these differences. Increased data acquisition
289 from both missions will enable a more reliable comparison of the mean SSHA from ICESat-2
290 and CryoSat-2.

291



292

293 **Figure 3:** Comparison between ICESat-2 and CryoSat-2 Arctic SSHA. **a)** time series of monthly
 294 mean SSHA for the Central Arctic (area outlined by green dashed-line in panel b) from ICESat-2
 295 (red) and CryoSat-2 (blue), with shaded areas representing one standard deviation from the

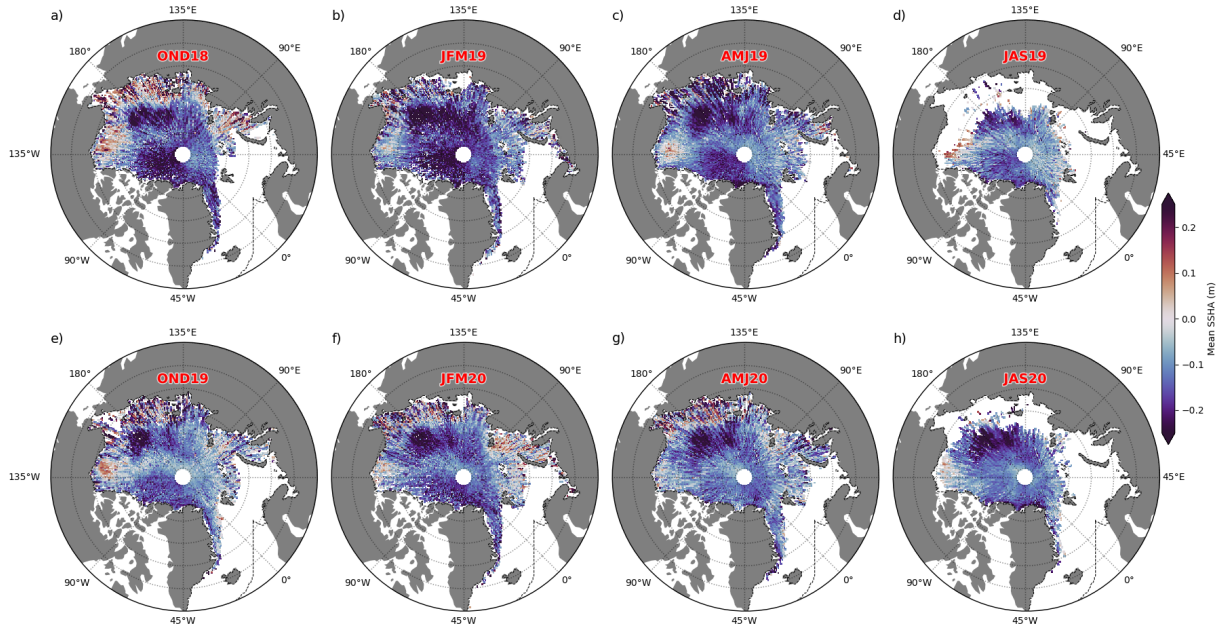
296 mean. **b-c)** Multi-year mean SSHA estimated using data acquired between November 2018 and
297 October 2020. **d)** Histogram showing the distribution of the differences between ICESat-2 and
298 CryoSat-2, also shown in map view in panel **e)**. In **d)** the black dash line marks the mean (μ) and
299 σ is the standard deviation. The black dashed line in **e)** marks the extent of the area of interest
300 (data outside this line are masked out).

301

302 *3.4 Seasonal SSHA variations from ICESat-2*

303 In Figure 4 we present seasonal maps of Arctic SSHA for three-month periods starting in
304 October 2018 and ending in September 2020. The top row (Figure 4a-d) can be directly
305 compared to the bottom row (Figure 4e-h) to assess year-to-year differences, while from left to
306 right we track the temporal progression during two entire freezing-melting seasons (2018–2019
307 and 2019–2020). Note that variations in spatial coverage are dictated by variations in sea ice
308 extent since ICESat-2 ATL10 data are only provided for areas that have an ice concentration >
309 50%. Comparisons to CryoSat-2 for each three-month period are presented in Figure S4, and
310 confirm similar SSHA spatio-temporal variations providing some confidence in the capability of
311 ICESat-2 to produce consistent estimates of Arctic SSHA.

312 A positive SSHA centered on the Beaufort Sea (a strengthened Beaufort Gyre) is clearly
313 visible during winter months but less apparent in 2020 (see Figure 4 c-d compared to Figure 4 g-
314 h). Large variability in the Siberian and Chukchi seas also corresponds to areas characterized by
315 high short-term SSH variability.



316

317 **Figure 4:** Seasonal mean SSHA maps from ICESat-2. OND = October, November, December;
 318 JFM = January, February, March; AMJ = April, May, June; JAS = July, August, September. The
 319 black dashed line marks the extent of the area of interest (data outside this line are masked out).

320

321 5 Summary and conclusions

322 Here we have presented a first examination of Arctic sea surface height anomalies
 323 (SSHA) from NASA's ICESat-2 laser altimeter during the first two years of the mission (2018-
 324 2020). We analyzed beam-to-beam differences and provided an independent assessment of inter-
 325 beam range biases for the ATLAS altimeter. We compared the ICESat-2 SSHA estimates with
 326 L2 sea ice data obtained from ESA's CryoSat-2 radar altimeter. We provided a brief description
 327 of the necessary steps to reconcile the SSHA data from the two altimetry missions by imposing
 328 the same permanent tide system, MSS, and geophysical corrections. A careful reconciliation of
 329 the data is needed in future efforts to blend data from ICESat-2 with those from CryoSat-2 (and
 330 potentially other airborne and space-borne altimetry missions).

331 The strong agreement between both the semi-synchronous along-track estimates from the
332 *CRYO2ICE* overlaps and basin-scale gridded SSHA estimates between the two sensors suggests
333 that the higher resolution ICESat-2 data can be used to estimate monthly/seasonal SSHA and
334 perhaps resolve 10 km-scale spatial variability in SSHA. The multi-year record of overlap also
335 opens up the potential to produce a new, high-resolution, blended, estimate of the mean sea
336 surface of the Arctic Ocean (and indeed Southern Ocean) which could better resolve what we
337 believe to be anomalously large SSHA spatial deviations shown in the *CRYO2ICE* overlaps.
338 Finally, our results provide a first evaluation of the approach used for the production of ICESat-2
339 SSHA gridded data products for the polar oceans (ATL21). Future work will extend this analysis
340 to the Southern Ocean, pending *CRYO2ICE* orbit maneuvers for the Southern Hemisphere.

341

342 **Acknowledgments, Samples, and Data**

343 ICESat-2 ATL10 data products were obtained from NSIDC and are available at
344 <http://nsidc.org/data/atl10>. CryoSat-2 Level-2 data (SIR_SAR_L2) were obtained from ESA at
345 <https://science-pds.cryosat.esa.int/#>. The mean sea surface grid is available at
346 <https://zenodo.org/record/4294048>.

347

348 **References**

349 Armitage, T. W. K., Bacon, S., & Kwok, R. (2018). Arctic Sea Level and Surface Circulation
350 Response to the Arctic Oscillation. *Geophysical Research Letters*, *45*(13), 6576–6584.
351 <https://doi.org/10.1029/2018GL078386>
352 Armitage, T. W. K., Bacon, S., Ridout, A. L., Thomas, S. F., Aksenov, Y., & Wingham, D. J.
353 (2016). Arctic sea surface height variability and change from satellite radar altimetry and
354 GRACE, 2003-2014: ARCTIC SSH VARIABILITY. *Journal of Geophysical Research: Oceans*,
355 *121*(6), 4303–4322. <https://doi.org/10.1002/2015JC011579>
356 Armitage, T. W. K., & Davidson, M. W. J. (2014). Using the Interferometric Capabilities of the
357 ESA CryoSat-2 Mission to Improve the Accuracy of Sea Ice Freeboard Retrievals. *IEEE*
358 *Transactions on Geoscience and Remote Sensing*, *52*(1), 529–536.
359 <https://doi.org/10.1109/TGRS.2013.2242082>
360 Armitage, T. W. K., Manucharyan, G. E., Petty, A. A., Kwok, R., & Thompson, A. F. (2020).
361 Enhanced eddy activity in the Beaufort Gyre in response to sea ice loss. *Nature Communications*,
362 *11*(1), 761. <https://doi.org/10.1038/s41467-020-14449-z>

- 363 Brunt, K. M., Smith, B. E., Sutterley, T. C., Kurtz, N. T., & Neumann, T. A. (2021).
364 Comparisons of Satellite and Airborne Altimetry With Ground-Based Data From the Interior of
365 the Antarctic Ice Sheet. *Geophysical Research Letters*, *48*(2).
366 <https://doi.org/10.1029/2020GL090572>
- 367 Giles, K.A., Laxon, S. W., Wingham, D. J., Wallis, D. W., Krabill, W. B., Leuschen, C. J.,
368 McAdoo, D., Manizade, S. S., & Raney, R. K. (2007). Combined airborne laser and radar
369 altimeter measurements over the Fram Strait in May 2002. *Remote Sensing of Environment*,
370 *111*(2–3), 182–194. <https://doi.org/10.1016/j.rse.2007.02.037>
- 371 Giles, Katharine A., Laxon, S. W., Ridout, A. L., Wingham, D. J., & Bacon, S. (2012). Western
372 Arctic Ocean freshwater storage increased by wind-driven spin-up of the Beaufort Gyre. *Nature*
373 *Geoscience*, *5*(3), 194–197. <https://doi.org/10.1038/ngeo1379>
- 374 Kwok, R., Kacimi, S., Markus, T., Kurtz, N. T., Studinger, M., Sonntag, J. G., Manizade, S. S.,
375 Boisvert, L. N., & Harbeck, J. P. (2019). ICESat-2 Surface Height and Sea Ice Freeboard
376 Assessed With ATM Lidar Acquisitions From Operation IceBridge. *Geophysical Research*
377 *Letters*, *46*(20), 11228–11236. <https://doi.org/10.1029/2019GL084976>
- 378 Kwok, R., Kacimi, S., Webster, M. A., Kurtz, N. T., & Petty, A. A. (2020). Arctic Snow Depth
379 and Sea Ice Thickness From ICESat-2 and CryoSat-2 Freeboards: A First Examination. *Journal*
380 *of Geophysical Research: Oceans*, *125*(3). <https://doi.org/10.1029/2019JC016008>
- 381 Kwok, R., & Morison, J. (2011). Dynamic topography of the ice-covered Arctic Ocean from
382 ICESat: DYNAMIC TOPOGRAPHY OF ARCTIC OCEAN. *Geophysical Research Letters*,
383 *38*(2), n/a-n/a. <https://doi.org/10.1029/2010GL046063>
- 384 Kwok, R., Petty, A. A., Bagnardi, M., Kurtz, N. T., Cunningham, G. F., Ivanoff, A., & Kacimi,
385 S. (2021). Refining the sea surface identification approach for determining freeboards in the
386 ICESat-2 sea ice products. *The Cryosphere*, *15*(2), 821–833. [https://doi.org/10.5194/tc-15-821-](https://doi.org/10.5194/tc-15-821-2021)
387 [2021](https://doi.org/10.5194/tc-15-821-2021)
- 388 Kwok, Ron, & Morison, J. (2016). Sea surface height and dynamic topography of the ice-
389 covered oceans from CryoSat-2: 2011–2014. *Journal of Geophysical Research: Oceans*, *121*(1),
390 674–692. <https://doi.org/10.1002/2015JC011357>
- 391 Kwok, Ron, Petty, A., Cunningham, G. F., Hancock, D. W., Ivanoff, A., Wimert, J. T., Bagnardi,
392 M., & Kurtz, N. (2020). *Algorithm Theoretical Basis Document (ATBD) For Sea Ice Products*.
393 Magruder, L. A., Brunt, K. M., & Alonzo, M. (2020). Early ICESat-2 on-orbit Geolocation
394 Validation Using Ground-Based Corner Cube Retro-Reflectors. *Remote Sensing*, *12*(21), 3653.
395 <https://doi.org/10.3390/rs12213653>
- 396 Meloni, M., Bouffard, J., Parrinello, T., Dawson, G., Garnier, F., Helm, V., Di Bella, A.,
397 Hendricks, S., Ricker, R., Webb, E., Wright, B., Nielsen, K., Lee, S., Passaro, M., Scagliola, M.,
398 Simonsen, S. B., Sandberg Sørensen, L., Brockley, D., Baker, S., ... Mizzi, L. (2020). CryoSat
399 Ice Baseline-D validation and evolutions. *The Cryosphere*, *14*(6), 1889–1907.
400 <https://doi.org/10.5194/tc-14-1889-2020>
- 401 Morison, J., Kwok, R., Dickinson, S., Andersen, R., Peralta-Ferriz, C., Morison, D., Rigor, I.,
402 Dewey, S., & Guthrie, J. (2021). The Cyclonic Mode of Arctic Ocean Circulation. *Journal of*
403 *Physical Oceanography*. <https://doi.org/10.1175/JPO-D-20-0190.1>
- 404 Morison, J., Kwok, R., Peralta-Ferriz, C., Alkire, M., Rigor, I., Andersen, R., & Steele, M.
405 (2012). Changing Arctic Ocean freshwater pathways. *Nature*, *481*(7379), 66–70.
406 <https://doi.org/10.1038/nature10705>
- 407 Neumann, T. A., Martino, A. J., Markus, T., Bae, S., Bock, M. R., Brenner, A. C., Brunt, K. M.,
408 Cavanaugh, J., Fernandes, S. T., Hancock, D. W., Harbeck, K., Lee, J., Kurtz, N. T., Luers, P. J.,

409 Luthcke, S. B., Magruder, L., Pennington, T. A., Ramos-Izquierdo, L., Rebold, T., ... Thomas,
410 T. C. (2019). The Ice, Cloud, and Land Elevation Satellite – 2 mission: A global geolocated
411 photon product derived from the Advanced Topographic Laser Altimeter System. *Remote*
412 *Sensing of Environment*, 233, 111325. <https://doi.org/10.1016/j.rse.2019.111325>

413 Peacock, N. R., & Laxon, S. W. (2004). *Sea surface height determination in the Arctic Ocean*
414 *from ERS altimetry*. 14.

415 Petty, A. A., Bagnardi, M., Kurtz, N., Tilling, R., Fons, S., Armitage, T., Horvat, C., & Kwok, R.
416 (n.d.). Assessment of ICESat-2 sea ice surface classification with Sentinel-2 imagery:
417 Implications for freeboard and new estimates of lead and floe geometry. *Earth and Space*
418 *Science*, n/a(n/a), e2020EA001491. <https://doi.org/10.1029/2020EA001491>

419 Polyakov, I. V., Pnyushkov, A. V., Alkire, M. B., Ashik, I. M., Baumann, T. M., Carmack, E. C.,
420 Goszczko, I., Guthrie, J., Ivanov, V. V., Kanzow, T., Krishfield, R., Kwok, R., Sundfjord, A.,
421 Morison, J., Rember, R., & Yulin, A. (2017). Greater role for Atlantic inflows on sea-ice loss in
422 the Eurasian Basin of the Arctic Ocean. *Science*, 356(6335), 285–291.
423 <https://doi.org/10.1126/science.aai8204>

424 Proshutinsky, A., Krishfield, R., Toole, J. M., Timmermans, M. -L., Williams, W., Zimmermann,
425 S., Yamamoto-Kawai, M., Armitage, T. W. K., Dukhovskoy, D., Golubeva, E., Manucharyan, G.
426 E., Platov, G., Watanabe, E., Kikuchi, T., Nishino, S., Itoh, M., Kang, S. -H., Cho, K. -H.,
427 Tateyama, K., & Zhao, J. (2019). Analysis of the Beaufort Gyre Freshwater Content in 2003–
428 2018. *Journal of Geophysical Research: Oceans*, 124(12), 9658–9689.
429 <https://doi.org/10.1029/2019JC015281>

430 Scagliola, M. (2013). *CryoSat footprints–Aresys Technical Note*. SAR-CRY2-TEN-6331,
431 Aresys/ESA, Italy.

432 Tilling, R., Kurtz, N. T., Bagnardi, M., Petty, A. A., & Kwok, R. (2020). Detection of Melt
433 Ponds on Arctic Summer Sea Ice From ICESat-2. *Geophysical Research Letters*, 47(23).
434 <https://doi.org/10.1029/2020GL090644>

435 Timmermans, M., & Marshall, J. (2020). Understanding Arctic Ocean Circulation: A Review of
436 Ocean Dynamics in a Changing Climate. *Journal of Geophysical Research: Oceans*, 125(4).
437 <https://doi.org/10.1029/2018JC014378>

438 Wingham, D. J., Francis, C. R., Baker, S., Bouzinac, C., Brockley, D., Cullen, R., de Chateau-
439 Thierry, P., Laxon, S. W., Mallow, U., Mavrocordatos, C., Phalippou, L., Ratier, G., Rey, L.,
440 Rostan, F., Viau, P., & Wallis, D. W. (2006). CryoSat: A mission to determine the fluctuations in
441 Earth's land and marine ice fields. *Advances in Space Research*, 37(4), 841–871.
442 <https://doi.org/10.1016/j.asr.2005.07.027>

443 Zwally, H. J., Schutz, B., Abdalati, W., Abshire, J., Bentley, C., Brenner, A., Bufton, J., Dezio,
444 J., Hancock, D., Harding, D., Herring, T., Minster, B., Quinn, K., Palm, S., Spinhirne, J., &
445 Thomas, R. (2002). ICESat's laser measurements of polar ice, atmosphere, ocean, and land.
446 *Journal of Geodynamics*, 34(3–4), 405–445. [https://doi.org/10.1016/S0264-3707\(02\)00042-X](https://doi.org/10.1016/S0264-3707(02)00042-X)

447 IPCC. *IPCC Special Report on the Ocean and Cryosphere in a Changing Climate* (IPCC, 2019).